

## A High-Accuracy Multiwavelength Radiometer for In Situ Measurements in the Thermal Infrared. Part II: Behavior in Field Experiments

GÉRARD BROGNIEZ, CHRISTOPHE PIETRAS,\* MICHEL LEGRAND, PHILIPPE DUBUISSON,<sup>+</sup>  
AND MARTIAL HAEFFELIN<sup>#</sup>

*Laboratoire d'Optique Atmosphérique, Université des Sciences et Technologies de Lille, Villeneuve d'Ascq, France*

(Manuscript received 11 March 2002, in final form 6 December 2002)

### ABSTRACT

The performances of the new conveyable low-noise infrared radiometer for measurements of atmosphere and ground surface targets, or CLIMAT, are presented for in situ measurements. For this, quantitative analyses were carried out on measurements performed with a prototype during various field experiments. The accuracy of the radiometric measurements controlled by using a field blackbody is estimated for severe environmental conditions. Two modes of operation and two types of targets are described. Ground-based measurements of the sky radiance are compared to radiative transfer calculations that use atmospheric profiles from radiosoundings as input parameters. Sea surface temperatures estimated from airborne CLIMAT measurements are compared to satellite retrievals. These experiments constitute a first set of quantitative tests of the CLIMAT radiometer for ground-based and airborne remote sensing applications. They demonstrate that CLIMAT can be considered for future studies on clouds and aerosols, sea water, and surface such as ice, vegetation, bare soil, and rocks.

### 1. Introduction

Several studies show the need for a well-characterized narrow field-of-view (FOV) infrared radiometer. Such an instrument would be very valuable for the study of clouds (e.g., Flamant et al. 1989), the study of vegetation for agronomy (e.g., Boissart et al. 1990; Seguin et al. 1991), the study of soil and rocks for pedology and geology (e.g., Nerry et al. 1990; Schmugge et al. 1991), and the study of desert dust emitted in arid areas such as the Sahara or Sahel (e.g., Fouquart et al. 1987). The conveyable low-noise infrared radiometer for measurements of atmosphere and ground surface targets or CLIMAT, is a multichannel infrared radiometer intended for such field measurements. Part I of this paper (Legrand et al. 2000) provides a technical description and a full laboratory characterization of the CLIMAT prototype. The calibration coefficients required to convert instru-

ment counts into radiances are derived from measurements made in the laboratory. A description of the calibration procedure and results are provided in Part I of the paper. Even though promising, the behavior observed in the laboratory cannot ensure that the instrument performances will be satisfactory when deployed in field operations.

Infrared measurements performed in the terrestrial environment are of two kinds: ground based (e.g., Platt and Dilley 1979; Flamant et al. 1989; Brogniez et al. 1995) and airborne (e.g., Saunders 1967; Lorenz 1968; Weiss 1971; Fouquart et al. 1987; Saunders and Minnet 1990). This work presents the performance of CLIMAT in both ground-based and airborne applications. For ground-based applications, a field blackbody was deployed to control the accuracy of the radiometer measurements. The control consists of comparing the blackbody temperature measured by a calibrated platinum resistor to the blackbody brightness temperature derived from radiometer measurements.

Ground-based field measurements were obtained during a field campaign that took place in the Sahel over several months of the dry season in 1998. The goal of the field campaign was to assess aerosol optical properties from brightness temperature measurements. The blackbody brightness temperature obtained from CLIMAT is compared to the platinum resistor measurements over a period of several months. The dataset is used to assess the instrument performance in the severe environmental conditions provided by the Sahel, that is,

\* Current affiliation: NASA Goddard Space Flight Center, Greenbelt, Maryland.

<sup>+</sup> Current affiliation: ELICO, Université du Littoral Côte d'Opale, Wimereux, France.

<sup>#</sup> Current affiliation: LMD, Ecole Polytechnique, Palaiseau, France.

*Corresponding author address:* Dr. Gérard Brogniez, Lab. D'Optique Atmosphérique UMR CNRS 8518, Université de Sciences et Technologies de Lille, U.F.R. de Physique-Batiment P5, Villeneuve d'Ascq Cedex F-59655, France.  
E-mail: gerard.brogniez@univ-lille.fr

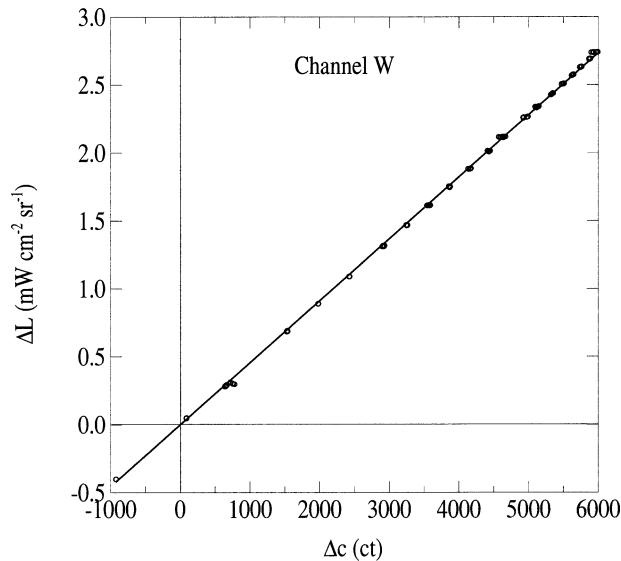


FIG. 1. Radiance calibration of channel W performed in Oct 1997 from (top right) 180 to (bottom left) 320 K,  $\Delta c$  is expressed in counts (ct). The zero value of  $\Delta c$  corresponds to the cavity temperature ( $\approx 295$  K).

strong diurnal temperature variations. A second set of field data was collected during a campaign in La Crau, in southeastern France, during July 1995. Clear-sky radiance measurements provide a good test case of low brightness temperature targets. CLIMAT brightness temperature retrievals are compared to radiative transfer code calculations that use radiosonde and sun photometer data as input.

The third test dataset comes from airborne measurements over the English Channel in June 1995. Sea surface temperatures (SSTs) are retrieved from CLIMAT multichannel brightness temperature measurements, using the split-window method to correct for atmospheric contributions. CLIMAT retrievals are compared to SST estimates from an operational space-borne sounding radiometer [the so-called along-track scanning radiometer (ATSR)]. These data allow us to test the behavior of CLIMAT when significant thermal gradients are present in the optical head of the radiometer due to the strong airflows.

The three field campaigns and the performance of CLIMAT through varying field conditions are presented in sections 2, 3 and 4. Conclusions on this first qualification of CLIMAT for in situ measurements are given in section 5.

## 2. General principle and main characteristics of the radiometer

The radiometer is made up of an optical head and a control unit. It is a portable, self-sufficient, and automated instrument. The optical head contains a thermopile inside an insulated (but not thermostated) cavity. The radiance coming from a target is measured through

TABLE 1. Global uncertainties in K (noises + biases) for two retrieved target brightness temperature (223 and 323 K) as a function of the detector temperature for 1-s measurements and for the four channels W, N12, N11, and N9.

Detector temperature	273 K		293 K		313 K	
	223 K	323 K	223 K	323 K	223 K	323 K
W	0.11	0.05	0.15	0.04	0.20	0.04
N12	0.29	0.13	0.33	0.12	0.38	0.12
N11	0.23	0.09	0.26	0.08	0.30	0.08
N9	0.28	0.07	0.30	0.07	0.33	0.07

a selected filter. It is compared with the blackbody radiance of the thermopile cavity, using a retractable golden mirror in front of the optical head. A detailed description of the instrument and its performance derived from laboratory measurements are given in Part 1 (Legrand et al. 2000). The main features of this instrument are

- three narrowband interference filters: N9 (8.2–9.2  $\mu\text{m}$ ), N11 (10.5–11.5  $\mu\text{m}$ ), N12 (11.5–12.5  $\mu\text{m}$ ), and a wide channel W (8–13.5  $\mu\text{m}$ );
- a field of view of  $10^\circ$ ;
- a measurement integration time of 1 s; and
- a typical radiometric noise on the order of 0.05 K (noise equivalent temperature difference; NEDT) for a 1- $\mu\text{m}$  bandwidth, at room temperature.

The radiometric calibration is performed by measuring the temperature and computing the corresponding radiance for a blackbody source in equilibrium. The conversion between radiance and brightness temperature is given by

$$L_i(T_i) = a_i \exp\left(-\frac{b_i}{T_i^{n_i}}\right), \quad (1)$$

where the parameters  $a_i$ ,  $b_i$ ,  $n_i$  characterize the spectral bandpass of each channel  $i$  (Table 4 in Legrand et al. 2000).

The relevant quantities are the difference in counts  $\Delta c_i$ , between the output signals of the radiometer viewing successively the blackbody and its own cavity, and the difference  $\Delta L_i$ , between the corresponding radiances. The radiometric sensitivity  $S_i$  is defined from the linear relation

$$\Delta c_i = S_i \Delta L_i, \quad (2)$$

for each channel  $i$ .

Figure 1 shows an example of a laboratory calibration that was used to determine the radiometric sensitivity in the channel W. The uncertainty on the determinations of  $S_i$  ranges between 0.25% and 0.05%. On the long term, the coefficients  $S_i$  showed only small variations ( $< 1.4\%$  over 7 months). The global uncertainties of the radiometer are recalled in Table 1 (from Legrand et al. 2000) for the four channels, three values of detector

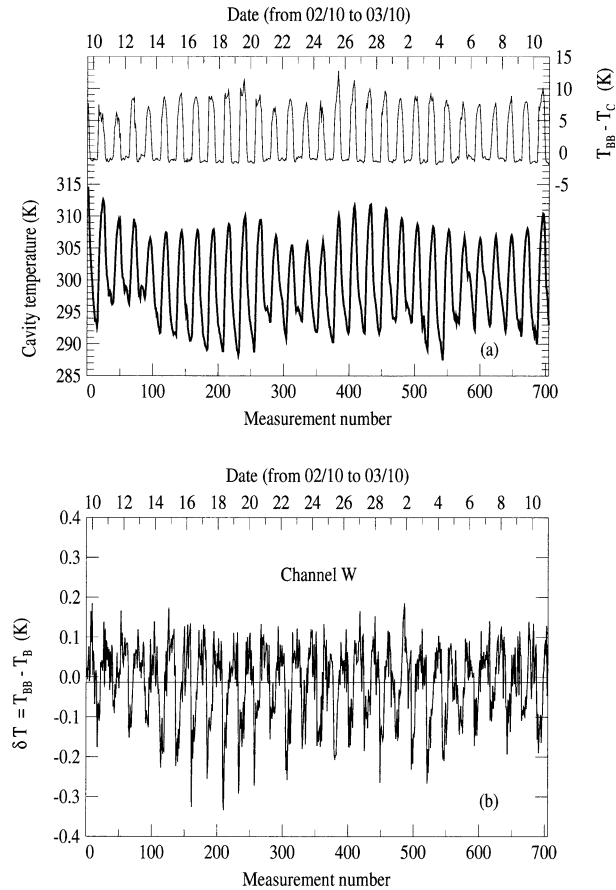


FIG. 2. [top: (a)] Diurnal cycle of the internal cavity temperature of the instrument for measurement made during a 30-day period in the Sahel. The difference between the blackbody temperature  $T_{BB}$  and the optical head cavity temperature  $T_c$  is also shown. [bottom: (b)] Diff  $\delta T$  between the blackbody temperature  $T_{BB}$  measured with the platinum probe and its brightness temperature  $T_B$  derived from radiometric measurements in channel W.

temperature, and two values of target temperature. The control of accuracy of the radiometric measurements in the field was performed by means of a field blackbody deployed with the radiometer.

### 3. Instrument accuracy in field measurements

CLIMAT was used in measurement campaigns extending at times over several months (in the Sahel in 1997 and 1998; India in 1999; Cape Verde in 2001; and China in 2001–02). These campaigns were dedicated to

aerosol studies. The objective was the remote sensing of desert dust by the instrument. Such an application is relevant, due to the presence in this aerosol of large particles ( $>1 \mu\text{m}$ ) that are detected in the thermal infrared. The instrument was associated with a field blackbody to verify that it was properly operating, and to allow measurements to be corrected in case the instrument sensitivity changed. The measurements of the radiometer viewing the blackbody are used with the calibration coefficients determined in the laboratory to derive the blackbody temperature. This brightness temperature is then compared to the temperature measured with the platinum probe inside the blackbody. We present here such measurements for a 4-month-long experiment carried out near Niamey, Niger, during the dry season (February–May 1998). The instrument was operating in the field in its automated mode, in a self-contained system. Its optical head was directed toward the target by a robot. The system was powered through a panel of solar cells. The measurements were collected once a week via a portable personal computer (PC). When doing a series of sky measurements, the radiometer viewed the blackbody and measured its radiance in order to validate the measurements.

Figure 2a shows the diurnal cycle of the internal cavity temperature  $T_c$  of the instrument for a series of 700 measurements (over a period of 30 days). Even though the optical head of the instrument is thermally insulated and painted white, the diurnal amplitudes are large (10–20 K) due to strong insolation. Figure 1a also shows the difference between the blackbody temperature  $T_{BB}$  and the cavity temperature  $T_c$ . This difference can exceed 10 K in the middle of the day because the blackbody is made of metal and coated with black paint.

As an example, Fig. 2b shows the corresponding difference  $\delta T$  in channel W between the temperature  $T_{BB}$  of the blackbody, measured with a platinum probe, and its brightness temperature  $T_B$ , derived from the radiometric measurements and from the instrument cavity temperature  $T_c$ . Table 2 presents the average radiance difference  $\overline{\delta L}$ , where  $\delta L = L(T_{BB}) - L(T_B)$  and standard deviation  $\sigma_{\delta L}$ , and the corresponding brightness temperature parameters  $\overline{\delta T}$  and  $\sigma_{\delta T}$ , for each of the four channels. We conclude from these results that the uncertainty of the brightness temperature measurements is on the order of 0.10 K, the instrument being subjected to strong diurnal thermal shocks. We note that these uncertainties are quite comparable to the corresponding estimates given in Table 1. For the objective of this

TABLE 2. Avg and std dev of (left half)  $\delta T$ , (right half) corresponding  $\delta L$ , and residuals  $\delta T_{res}$  and  $\delta L_{res}$  after correction of the diurnal biases  $\langle \delta T \rangle$  and  $\langle \delta L \rangle$  (see text). Sampling of 100 measurements (4 days) from the measurements shown in Fig. 2.

( $10^{-2}$ K)	$\overline{\delta T}$	$\sigma_{\delta T}$	$\overline{\delta T_{res}}$	$\sigma_{\delta T_{res}}$	( $\mu\text{W cm}^{-2} \text{ sr}^{-1}$ )	$\overline{\delta L}$	$\sigma_{\delta L}$	$\overline{\delta L_{res}}$	$\sigma_{\delta L_{res}}$
W	-1.37	9.37	0.0004	5.41	W	-0.98	5.19	-0.0143	2.93
N12	-2.50	11.20	0.00001	10.29	N12	-0.21	0.97	0.0002	0.88
N11	-5.16	10.48	-0.0516	7.34	N11	-0.68	1.32	-0.0050	0.92
N9	-0.38	8.34	-0.0571	7.39	N9	-0.03	0.79	-0.0050	0.70

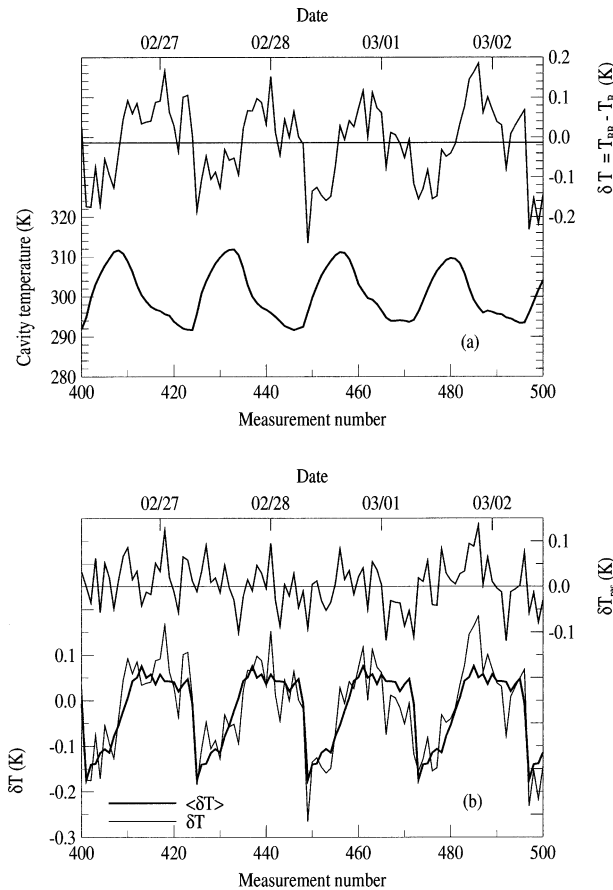


FIG. 3. [top: (a)] Comparison of the periodic behavior of the cavity temperature  $T_C$  with  $\delta T$  for a series of 100 measurements (see text). [bottom: (b)] Corresponding residual signal  $\delta T_{\text{res}}$ , which is the difference between  $\delta T$  and the solar time average value  $\langle \delta T \rangle$  of  $\delta T$ .

experiment, which is remote sensing of mineral dust, we consider this level of accuracy satisfactory, and no extra correction is needed.

However, Fig. 2 shows that a part of the amplitude of  $\delta T$  (Fig. 2b) is related to the diurnal temperature cycle itself (Fig. 2a). The 24-h component of this signal is a bias that can arise from

- 1) the thermal inertia of the blackbody,
- 2) the effect on the radiometer of the diurnal thermal shock [larger than the 10 K applied to the radiometer in the laboratory experiment described by Legrand et al. (2000)],
- 3) an uncertainty on the temperature dependence of the thermopile responsivity given by the manufacturer, or
- 4) slight errors on the values of the calibration coefficients used.

Figure 3a compares cycles of the cavity temperature  $T_C$  with cycles of  $\delta T$ . Indeed, it shows that the signals are shifted so that the maxima and minima of  $\delta T$  correspond with the largest diurnal heating and cooling rates of the cavity, respectively. This is in agreement

with hypotheses 1) and 2) above, which apparently explain the 24-h periodic component of  $\delta T$  (or most of it). Figure 3b shows the residual signal  $\delta T_{\text{res}} = \delta T - \langle \delta T \rangle$  where  $\langle \delta T \rangle$  is the periodic signal obtained by averaging  $\delta T(t)$  at every hour over the 30-day period. Table 2 presents the corresponding average and standard deviation of this residual signal, showing a vanishing bias and a slightly improved standard deviation ( $\leq 0.10$  K). These slight uncertainties have to be analyzed if especially accurate results were necessary, for example, by insulating the blackbody and the optical head in order to keep their temperatures uniform and constant.

#### 4. Ground-based measurements of the sky radiance

##### a. Description and objective of the experiment

Measurements of sky downwelling infrared radiance from zenith were performed in southeastern France as part of a field experiment conducted by the Institut National de la Recherche Agronomique (INRA). This campaign was dedicated to the comparison of the performances of various sensors, and to the analysis of environmental perturbations for applications in agrometeorology, forestry, and geology. The prototype CLIMAT was operated from 6 to 15 July 1995, in the plain of La Crau (43.68°N, 4.63°E), near the Mediterranean Sea. Sun photometric measurements in the short-wave range were performed at the same site. Balloon radiosoundings launched daily at the regional meteorological station of Nîmes (43.83°N, 4.31°E) 40 km away, gave the opportunity to compare the radiometric sky measurements to the corresponding simulations based on the vertical atmospheric profiles.

##### b. Measurements

We analyze hereafter, as an example, the results obtained for 12 July at the La Crau site. That day was observed to be clear in the field of view of the instrument, with, however, a slight veil of cirrus clouds as reported from the Météo-France weather station of Nîmes (2/8 of cirrus cloud cover). Sun photometric measurements were performed on that day at wavelengths  $\lambda_1 = 443$  nm and  $\lambda_2 = 870$  nm (Vermeulen 1996). The atmospheric optical thicknesses,  $\delta_{\lambda_1}$  and  $\delta_{\lambda_2}$ , derived from these measurements, after removal of the molecular component, are displayed in Fig. 4. From these two optical thicknesses, we derive the Ångström exponent  $\alpha$  of atmospheric particles given by the following equation:

$$\alpha = \frac{\ln(\delta_{\lambda_1}/\delta_{\lambda_2})}{\ln(\lambda_2/\lambda_1)}. \quad (3)$$

The values of  $\alpha$  are added to Fig. 4. The exponent  $\alpha$  computed from  $\delta_{443}$  and  $\delta_{870}$  is nearly constant between 0955 and 1045 UTC, with a value of about 1.4, which

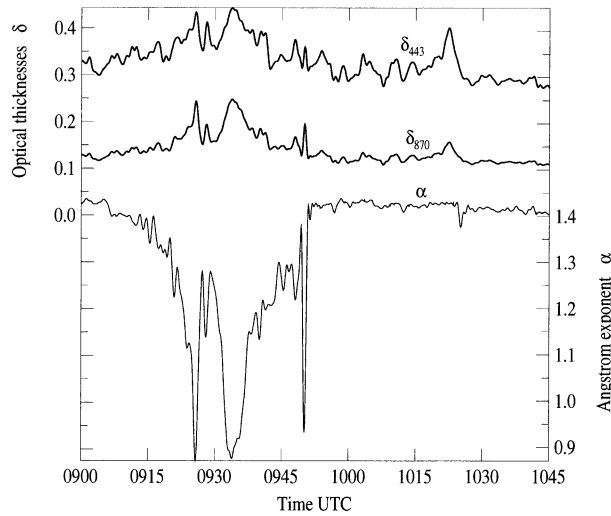


FIG. 4. Optical thickness  $\delta_{443}$  and  $\delta_{870}$  of the atmosphere, after subtracting the molecular component. Measurements obtained at La Crau, during the morning of 12 Jul 1995. Angstrom exponent  $\alpha$  calculated from  $\delta_{443}$  and  $\delta_{870}$  is added.

is typical for atmospheric aerosol usually observed in the midlatitudes. On the contrary, between 0910 and 0955 UTC the  $\alpha$  value falls down to 0.9, indicating the presence of large particles probably due to a cirrus cloud in the sun photometer FOV.

Infrared radiometric measurements of the zenithal sky radiance were obtained between 0830 and 1350 UTC. The radiometric records of channels W, N12, N11, and N9 are shown in Fig. 5a for the downward radiance and in Fig. 5b for the corresponding brightness temperature of sky, using the calibration coefficients of 27 July 1995 (Table 5 in Legrand et al. 2000) and the radiance-brightness temperature fit [Eq. (1)]. Between 0910 and 0955 UTC, the radiometric signals shown in Fig. 5 appears steadier than the sun photometric signals of Fig. 4. On the contrary, after 0955 UTC the photometric signal becomes smoother, while the radiometric signals fluctuate over several kelvins. These discrepancies between the signal behaviors are due to the fact that CLIMAT is directed toward zenith, while the photometer aims at a low-elevation sun (early in the morning). So it is not clear from Fig. 5 whether semitransparent cirrus clouds passed overhead or not in the FOV of the radiometer.

*c. Measured and modeled infrared sky radiances*

Mean radiances and brightness temperatures derived from CLIMAT measurements (averaged over 0910–0955 UTC 12 July 1995) are shown in column 2 of Table 3, along with the  $2\sigma$  intervals ( $\pm 2\sigma_L$  and  $\pm 2\sigma_r$ ).

The radiance and the corresponding brightness temperature have been calculated using a line-by-line model, from the atmospheric profiles given by radiosounding measurements from the station at Nîmes. Figure 6 shows the atmospheric profiles of temperature and relative hu-

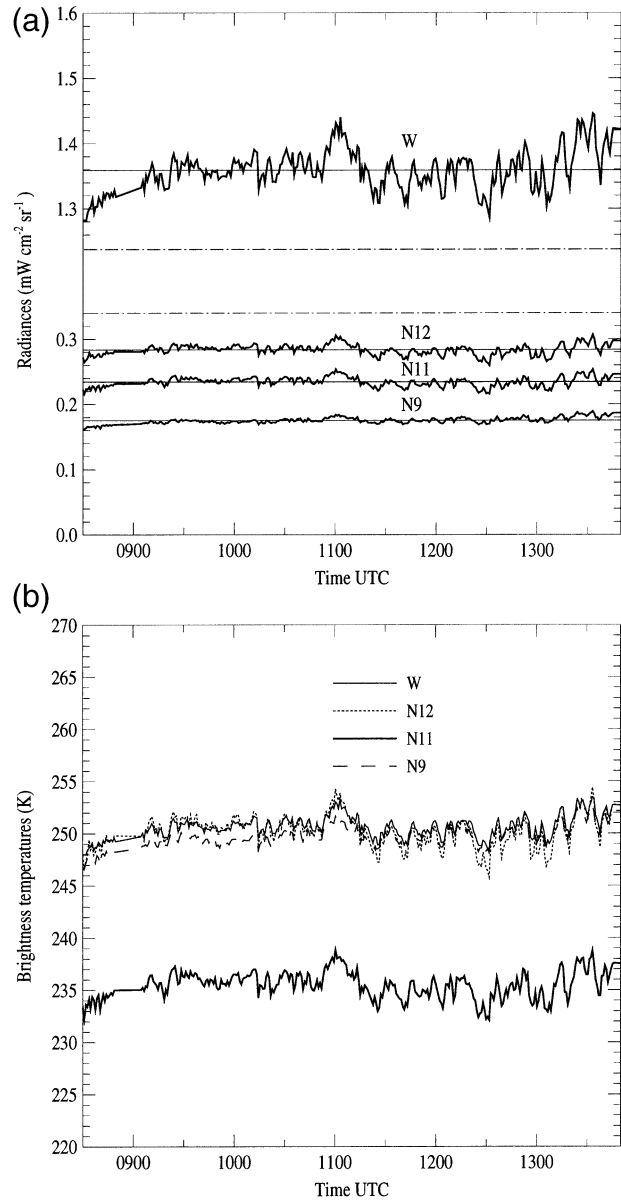


FIG. 5. Sky radiometric measurements with the four channels of CLIMAT for 12 Jul 1995. (a) Zenithal radiances (the horizontal lines correspond to mean radiance values of the record) and (b) corresponding brightness temperatures are shown.

midity from the sounding launched at 1115 UTC. The balloon ascent lasted about 1 h. Above the maximum height of the available data (9500 m), the atmospheric profiles were extrapolated with a midlatitude summer model (McClatchey et al. 1971). The humidity profile did not indicate presence of any cirrus clouds, however, such clouds could be above 9500 m.

The line-by-line model (Dubuisson et al. 1996) simulates the downwelling radiance through a pure gaseous atmosphere. The spectroscopic database of the model includes the 1996 High-resolution Transmission Model (HITRAN-96) (Rothman et al. 1998) and the continuum

TABLE 3. Mean values and  $2\sigma$  intervals derived from the record set of radiance and brightness temperature in the four channel of the radiometer (campaign of La Crau, Jul 1995). Simulations for clear atmosphere are reported in the third column of each set. Results for a 5% increased humidity are reported in the fourth column. The effects of aerosols are added in the fifth column. The effects of a cirrus cloud with a visible optical thickness value equal to 0.02 are added in column 6. In the last column of each set, we have reported the total effect of column 6 after replacing C K D-2.2 and HITRAN 96 by C K D-2.4 and HITRAN 2000 spectroscopic database.

	$L_{\text{measured}} (2\sigma_L)$ ( $\text{mW cm}^{-2} \text{sr}^{-1}$ )		$L_{\text{simulated}} (\text{mW cm}^{-2} \text{sr}^{-1})$					$T_{\text{measured}} (2\sigma_T)$ (K)	$T_{\text{simulated}}$ (K)	
	Gaseous (CKD-2.2 HITRAN 96)	+5% WV	+ Aerosol ( $\delta = 0.32$ )	+ Cirrus ( $\delta = 0.02$ )	Total effect us- ing CKD-2.4 and HITRAN 2000	Gaseous (CKD-2.2 HITRAN 96)	+5% WV			+ Aerosol ( $\delta = 0.32$ )
W	1.355 (0.064)	1.222	1.246	1.360	1.349	243.82	245.76	246.65	250.75	250.34
N12	0.284 (0.016)	0.281	0.284	0.304	0.303	246.95	249.53	250.11	254.51	254.32
N11	0.234 (0.014)	0.205	0.225	0.248	0.245	230.04	232.71	233.48	238.13	237.54
N9	0.175 (0.008)	0.135	0.147	0.167	0.165	239.89	241.16	242.75	247.89	247.35

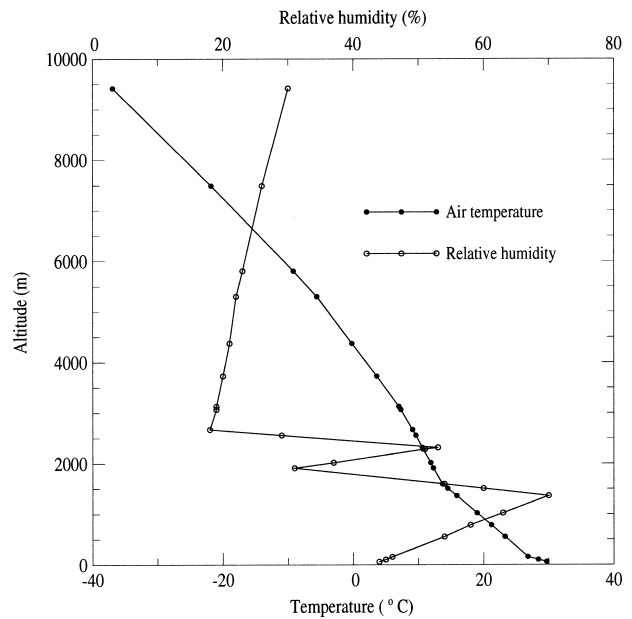


FIG. 6. Atmospheric profiles of temperature and relative humidity obtained from the balloon sounding launched at Nîmes, at 1115 UTC 12 Jul 1995.

parameterization of Clough et al. (1989, 1992) for water vapor absorption, with the CKD-2.2 water vapor model. Gaseous species having a weak effect, such as ozone ( $\text{O}_3$ ), carbon dioxide ( $\text{CO}_2$ ), nitrogen dioxide ( $\text{NO}_2$ ), and methane ( $\text{CH}_4$ ) are included in the model. These simulations are shown in the third column of Table 3.

The comparison of columns 2 and 3 of Table 3 shows that the model calculations produce lower brightness temperatures than those derived from measurements. Difference varies from 3.15 K for channel N12 to 9.65 K for channel N9. The mean measured brightness temperatures, and the calculated brightness temperatures are displayed in Fig. 7 for each channel. The corresponding  $\pm 2\sigma_T$  intervals are displayed also in Fig. 7.

d. Discussion

Discrepancies between measurements and model calculations can be explained by several uncertainties: 1) radiometric measurements uncertainties, 2) uncertainties in model and spectroscopic data for water vapor in the line-by-line model, 3) uncertainties in the atmospheric profiles, 4) the presence of aerosols, and 5) the presence of cirrus clouds.

1) RADIOMETRIC MEASUREMENTS UNCERTAINTIES

We showed (Table 1 and Fig. 3a) that brightness temperatures can be estimated from CLIMAT measurements with an uncertainty on the order of 0.10 K for temperatures ranging from 290–320 K. For sky measurements in the range 230–250 K. Table 1 shows an increased uncertainty of 0.20–0.25 K. Nevertheless, these values

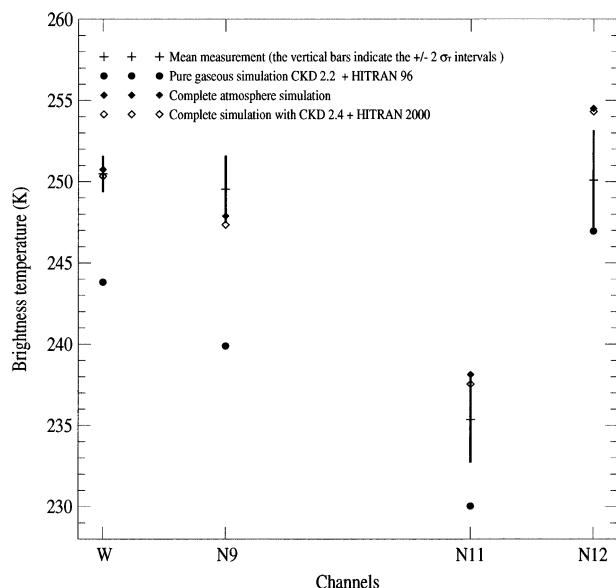


FIG. 7. Brightness temperature comparisons between measurements and simulations at the frequency of the four channels of the radiometer.

are small compared to the differences between measurements and simulations shown in Fig. 7.

## 2) ATMOSPHERIC PROFILE UNCERTAINTIES

Radiosonde sensors are known to significantly underestimate the relative humidity. Comparisons made by Météo-France between sensors Vaisala RS80 and RS90, show differences between 5% and 10% (J. L. Gaumet 2001, personal communication). So, we can expect relative humidity errors to be in the  $-5\%$  to  $-10\%$  range. The line-by-line computations (using CKD-2.2 and HITRAN-96) are computed with a relative humidity profile increased by 5%. Results are reported in the fourth column of Table 3. The increased relative humidity yields increased brightness temperatures ranging from 1.3 (channel N9) to 2.7 K (channel N11).

## 3) AEROSOL EFFECT

The effect of aerosols on radiative transfer calculations is investigated using sun photometric measurements. At 1000 UTC 12 July, the aerosol optical thickness is estimated to be 0.32 at 440 nm (Fig. 4). The LOWTRAN-7 code (Kneizys et al. 1988), that includes a package with several aerosol models, is used instead of the line-by-line model. We select the rural aerosol model with a 23-km visibility that is well-suited to the environmental conditions of the experiment. For a visibility of 23 km its optical thickness at 550 nm is 0.32 (to be compared to 0.32 measured at 440 nm). This calculated aerosol effect should be added to the simulated values of the pure gaseous atmosphere given by the line-by-line model. Results are reported in the fifth

column of Table 3. The brightness temperature is increased from 0.6 (channel N12) to 1.6 K (channel N9).

## 4) CIRRUS CLOUD EFFECT

The presence of cirrus clouds during the experiment was revealed by the meteorological synoptic observations, and by the Ångström exponent derived from sun photometric measurements. Nevertheless, the presence of such clouds in the radiometer FOV is not obvious, and cannot be ensured. However, we compute the effect of a thin cirrus using the LOWTRAN-7 code (subvisual cirrus at an altitude of 10 km). For a cirrus optical thickness of 0.02 at 550 nm, the brightness temperature presented in column 6 of Table 3 shows significant increases varying between 4.4 (channel N12) and 5.1 K (channel N9). The signal increase of 3–4 K observed at 1100 UTC on Fig. 5b could be explained by such cirrus.

## 5) MODEL AND SPECTROSCOPIC DATA FOR WATER VAPOR

In the  $10\text{-}\mu\text{m}$  atmospheric window, water vapor is the main radiatively active gaseous component. For the calculations, the water vapor effect is considered to be the sum of weak lines and a continuum, the description of which involves uncertainties. So, the use of continuum models CKD-1 and CKD-2.2 results in differences of brightness temperatures as large as 8 K in channel N11 for a wet tropical atmosphere (Han et al. 1997). We have investigated the order of magnitude of the uncertainty associated to the use of the CKD-2.2 and HITRAN-96 database by replacing them by the new CKD-2.4 and HITRAN-2000 data (Tobin et al. 1999; Giver et al. 2000; Rothman et al. 2001). The results are shown in the last column of Table 3. The new values are systematically lower. The maximum deviation is  $-0.59$  K for channel N11.

## e. Comments

In Fig. 7, we report the simulated brightness temperatures obtained from

- 1) the line-by-line model with the CKD-2.2 and HITRAN 96 water vapor data;
- 2) the combined effects of a 5% increase in relative humidity, rural aerosol model with an optical thickness of 0.32 at 550 nm (in agreement with sunphotometer measurements), and subvisual cirrus cloud with an optical thickness of 0.02 at 550 nm, and
- 3) the input parameters of 2) combined with the new CKD-2.4 and HITRAN 2000 database, instead of CKD-2.2 and HITRAN 96.

In Fig. 7, the underestimation of the measured radiances by the computations observed in case 1) above, dis-

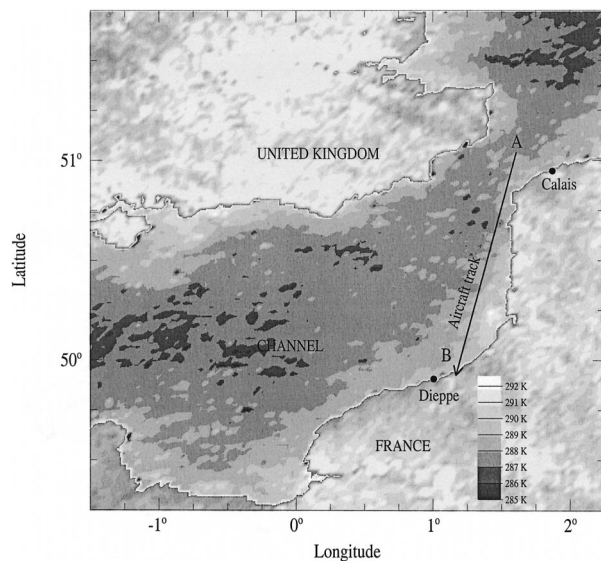


FIG. 8. Map of field campaign area: sea surface temperature over the English Channel at 1106 UTC 28 Jun 1995 is derived from ATSR-1 on board ERS-1. The aircraft track A–B is superimposed.

appears in cases 2) and 3). We should note that the cirrus clouds give rise to both the largest effect (4.4–5.1 K) and the largest uncertainties (amount in the radiometer FOV, spectral radiative properties). The relative humidity profile is the second case, as to its effect (1.3–2.7 K) and its uncertainties (on the performances of the sensors). Nevertheless, the combination of the various effects involved shows the possibility of an overall agreement between measurements and simulations. In addition, it must be stressed that radiometric measurement uncertainties (maximum of 0.25 K) are small compared to the effects discussed above. Figure 7 reveals also the different behaviors of the various radiometer channels. In cases 2) and 3) above, the simulations underestimate the measurements in channel N9, while they overestimate them in channels N11 and N12. On the other hand, in channel W the simulations agree with the measurements, which is consistent with the average operated by this channel.

## 5. Airborne measurements of sea surface temperature

### a. Description and objective of the campaign

In order to check the stability and noise of the instrument for airborne operations, the prototype CLIMAT was flown on board a Piper PA28 Arrow 4, next to a Barnes precision radiation thermometer (PRT-5), with both instruments viewing at nadir through an opening in the aircraft floor. The optical head of the prototype CLIMAT was not particularly protected against possible temperature perturbations due to the airflow.

In addition, we took advantage of this campaign to assess the multichannel capabilities of the instrument

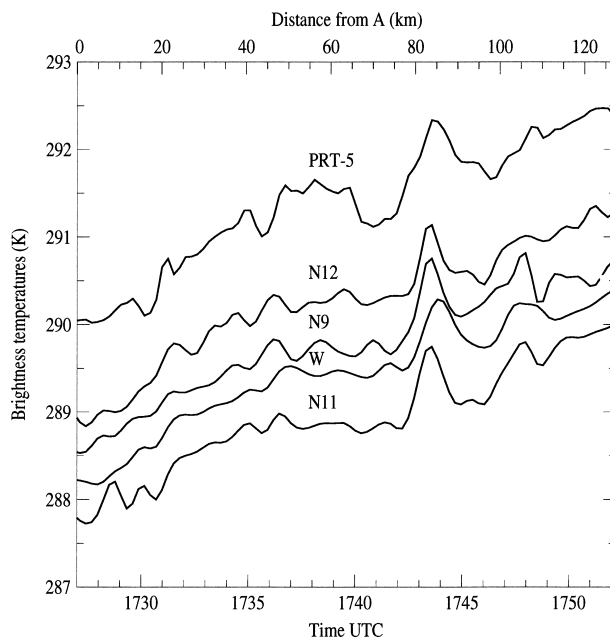


FIG. 9. Brightness temperatures of the sea surface along the A–B leg (Calais–Dieppe) that are derived from measurements of PRT-5 and CLIMAT.

for the determination of the sea skin temperature, which is an important parameter for meteorology and climatology. For that purpose, the instrument was flown during the clear day of 28 June 1995 at an altitude of about 750 m above the English Channel. We performed the flight along a transect off of the French coast, as depicted in Fig. 8, from a point “A” (51.03°N, 1.62°E) near Calais to a point “B” (49.92°N, 1.17°E) near Dieppe.

### b. Presentation of measurements and discussion

The measurements were acquired by both radiometers, at 1-Hz frequency. Figure 9 shows an example of the sea brightness temperatures measured from 1725 to 1755 UTC with the PRT-5 and with the four channels of CLIMAT as a function of the distance along the A–B leg. A temporal filter was applied to the data from the PRT-5 to account for its narrow FOV (2° versus 10° for CLIMAT). The variations of brightness temperature measured by both instruments along the A–B leg are similar. The absolute values of the brightness temperatures are different due to the wavelength-dependent contributions of the atmosphere (water vapor) and of the surface (sea water emissivity). Channel N11 corresponds to the most transparent part of the (8–13  $\mu\text{m}$ ) infrared atmospheric window (Fig. 3 in Legrand et al. 2000), and it coincides with the maximum sea water emissivity (Masuda et al. 1988). It provides a brightness temperature  $T_{11}$  closer to the surface temperature  $T_s$  than  $T_{12}$  and  $T_9$  (corresponding to channels N12 and N9). The departure is larger for the PRT-5 channel with full width at half maximum (8–14  $\mu\text{m}$ ) and a bandpass ex-

tending up to 16  $\mu\text{m}$ , widely overlapping the 15- $\mu\text{m}$  carbon dioxide absorption band. The relative values of the measured brightness temperature shown in Fig. 9 reveal that the sea surface was colder than the air layer below the flight level. So,  $T_s$  must be lower than all the brightness temperatures shown in Fig. 9.

1) DESCRIPTION OF THE SPLIT-WINDOW METHOD

The radiative transfer equation gives the radiance  $L_i^{\text{RAD}}$  measured by the radiometer in the channel  $i$  in terms of sea surface and atmospheric temperatures, sea surface emissivity, and atmospheric transmittance. The atmospheric transmittance depends on the atmospheric profiles of the absorbing and scattering species. For nadir viewing, and neglecting the scattering, we can write

$$L_i^{\text{RAD}} = \epsilon_i t_i L_i^\uparrow(T_s) + \int_{t_i}^1 L_i^\uparrow(T) dt + (1 - \epsilon_i) t_i \int_1^{t_i^\#} L_i^\downarrow(T) dt, \quad (4)$$

where  $\epsilon_i$  is the sea surface emissivity,  $t_i$  is the transmittance of the atmospheric layer between the surface and the radiometer,  $t_i^\#$  is the transmittance of the complete atmosphere,  $\epsilon_i L_i^\uparrow(T_s)$  is the upwelling radiance emitted by the surface at the temperature  $T_s$ , and  $L_i^\uparrow(T)$  and  $L_i^\downarrow(T)$  are, respectively, the upwelling and downwelling radiances in the atmosphere at a given level where the temperature is  $T$ . The first term of this equation corresponds to the radiance emitted by the surface. The second term is the upwelling radiance emitted by the atmosphere. The third term corresponds to the downwelling atmospheric radiance reflected by the surface up to the radiometer.

For the atmospheric correction, the ‘‘split-window’’ techniques are based on the differential atmospheric transmittance between two channels. Channels centered at 11 and 12  $\mu\text{m}$  are well known to be suitable for this purpose, and the skin temperature may be derived as a combination of the 11- and 12- $\mu\text{m}$  brightness temperatures. Starting from Eq. (4) for channels N11 and N12, we replace the radiances by brightness temperatures and expand the blackbody function in a Taylor’s series around  $T_s$ , up to the second order. The ‘‘global split-window’’ formula (Franois and Ottle 1994) can be derived in this manner. It appears as a quadratic dependence of  $(T_s - T_{11})$  with  $(T_{11} - T_{12})$ :

$$T_s - T_{11} = \alpha(T_{11} - T_{12}) + \beta(T_{11} - T_{12})^2 + \gamma. \quad (5)$$

For the channels N11 and N12 of CLIMAT, simulated values of brightness temperatures of the sea surface were computed at the aircraft altitude with

- 1) sea surface emissivities at nadir (with weak or moderate wind),  $\epsilon_{11}$  and  $\epsilon_{12}$  in channels N11 and N12, respectively, given by Masuda et al. (1988):

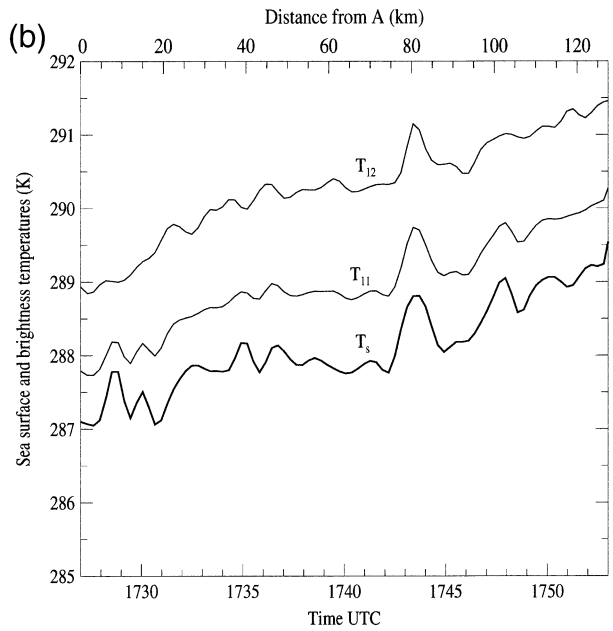
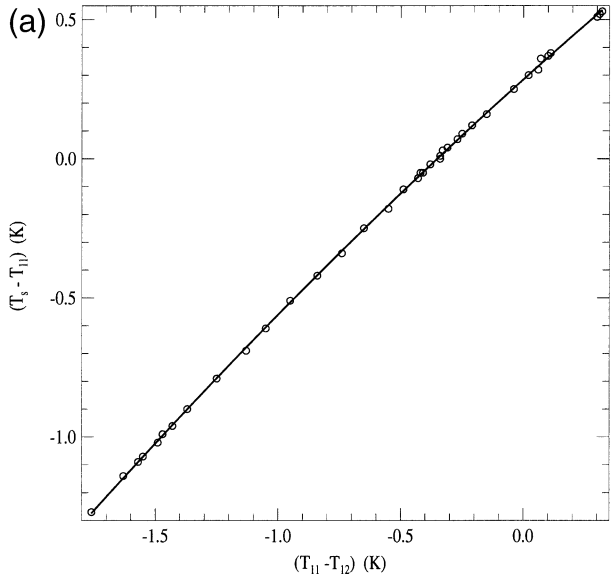


FIG. 10. (a) Scatterplot and quadratic fit of  $(T_s - T_{11})$  as a function of  $(T_{11} - T_{12})$  obtained from the LOWTRAN-7 code with 39 different sea surface temperatures and atmospheric conditions. (b) Retrieval of the sea surface temperature  $T_s$ , from the brightness temperatures  $T_{11}$  and  $T_{12}$  measured by CLIMAT.

$$\epsilon_{11} = 0.9925, \quad \epsilon_{12} = 0.9889, \quad \text{and}$$

- 2) sets of sea surface temperatures and atmospheric profiles of temperature and humidity (39 different datasets were considered).

For each dataset, using the LOWTRAN-7 code, we compute the brightness temperatures  $T_{11}$  and  $T_{12}$ . The plot  $(T_s - T_{11})$  as a function of  $(T_{11} - T_{12})$  is presented in Fig. 10a along with a quadratic fit. These results are used to derive the values of  $\alpha$ ,  $\beta$ , and  $\gamma$  in Eq. (5):

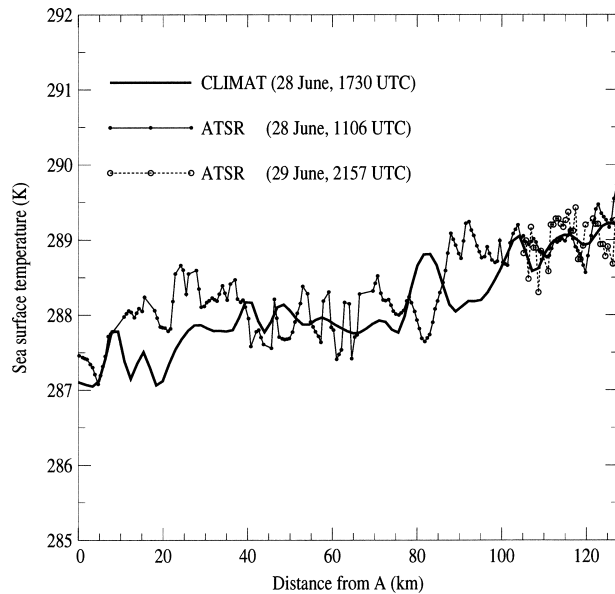


FIG. 11. Comparisons of the sea surface temperature given by CLIMAT and by ATSR along the aircraft track A–B, as a function of the distance from A.

$$\alpha = +0.7937, \quad \beta = -0.0524 \text{ K}^{-1},$$

$$\gamma = +0.2855 \text{ K}.$$

The fit allows  $T_s$  to be retrieved from measured values of  $T_{11}$  and  $T_{12}$ , with a standard error of about 0.02 K.

Figure 10b shows the sea surface temperature  $T_s$  retrieved from Eq. (4). The brightness temperatures from channels N11 and N12 are added for comparison. As previously predicted,  $T_s$  is lower than either brightness temperatures.

## 2) COMPARISON WITH ATSR/ERS-1 RETRIEVAL

The retrieved values of sea surface temperature were compared with the values derived from satellite data. We used sea surface temperature derived from images of the ATSR/*European Remote Sensing Satellite-1* (ERS-1) (Mutlow et al. 1994) acquired over the English Channel at 1106 UTC 28 June (Fig. 8). These data, whose accuracy is  $\pm 0.3$  K, are provided by the Rutherford Appleton Laboratory. They are derived from satellite measurements by application of the synthesis of ATSR data into sea surface temperature (SADIST) data-processing scheme (Bailey 1994). More specifically, we analyzed the pixels located along the aircraft track. In Fig. 11, we report the sea surface temperatures derived from ATSR and from CLIMAT as a function of the distance along the A–B leg for the pixels coinciding with the aircraft track. Despite the different spatial resolutions of ATSR and CLIMAT ( $\approx 1$  km and  $\approx 125$  m, respectively), and the time difference between satellite and aircraft measurements ( $\approx 1100$  and  $\approx 1730$  UTC, respectively), the two time series of sea surface tem-

perature appear to be in good agreement. Along the A–B leg, the mean difference between the temperatures derived from ATSR and CLIMAT is 0.19 K with a standard deviation of 0.44 K.

In addition, we have considered the sea surface temperature from the next ATSR/ERS-1 dataset, corresponding to an image acquired at 2157 UTC 29 June. Only the last 20 km of the A–B leg are available, at the limit of the instrument swath, as shown in Fig. 11. In this part of the leg, the temperature retrieval agrees well with CLIMAT measurements, with a mean difference of 0.01 K and a standard deviation of 0.55 K. This reveals that in the area of the experiment, the sea surface temperature was rather stable in the 28–29 June period, which resulted in good experimental conditions for CLIMAT and ATSR comparisons.

## 6. Conclusions

Three measurement campaigns carried out with a prototype of the new CLIMAT are presented in order to assess its performance when operated at ground level or from an aircraft. In a first campaign carried out in the Sahel during the dry season, which involved severe environmental conditions, the radiometer measurements, were validated using a blackbody. The difference between the values of blackbody temperatures, measured with a platinum probe and those derived from radiometric measurements, is approximately 0.1 K in all channels. This error results partly from the strong temperature shift associated with the diurnal cycle and could be corrected. This first test clearly demonstrates the reliability of the instrument operated in situ and the accuracy of its measurements.

A second ground-based campaign was performed in La Crau to measure sky brightness temperatures in the different channels of the radiometer. The comparisons between the radiances (or the brightness temperatures), measured and calculated with a line-by-line model, show an overall agreement, with, however, noticeable differences depending on the channel. The analysis shows that the uncertainties are mostly of atmospheric origin. To reduce these uncertainties, it would be advisable to repeat such a campaign with an enhanced instrumentation set, including a sun photometer and a backscattering lidar, several types of humidity sensors, and collocated satellite data.

A third campaign was carried out in order to investigate the performances of the prototype mounted on board an aircraft. The nadir-looking instrument was flown over the English Channel, measuring the brightness temperatures in the two channels centered at 11 and 12  $\mu\text{m}$ . The quadratic split-window method was used to retrieve the skin temperature of the sea. The results are in good agreement with the sea surface temperatures derived from ATSR on board the ERS-1 satellite.

These three experiments constitute a first set of quan-

titative tests of the CLIMAT radiometer for in situ measurements. They reveal that CLIMAT is a suitable instrument for studies involving multichannel capabilities in a variety of fields in ground-based and airborne operating modes. The radiometer can be used alone or jointly with satellite remote sensing to improve satellite data analysis.

Further studies and experiments will help to better characterize the capabilities, limits, and shortcomings of CLIMAT. But we may already consider that this instrument can be very useful for the scientific community.

*Acknowledgments.* This work was supported by the Centre National d'Etudes Spatiales (CNES) under Contract 93/CNES/0373. Thanks are due to J. P. Buis and G. Clave from CIMEL Electronique, who participated very actively in the radiometer manufacturing. The authors are very grateful to G. Guyot for the management of the campaign of La Crau, and to C. Verwaerde, J. Y. Balois, and C. Devaux, for their assistance during field experiments. Thanks are also due to N. Houghton from the Rutherford Appleton Laboratory, England, who provided us with the sea surface temperatures derived from ATSR. Thanks are also due to M. Tavet for correcting the English text and to the two referees for their constructive remarks and comments.

## REFERENCES

- Bailey, P., 1994: SADIST products (version 600). Space Science Department, Rutherford Appleton Laboratory, 99 pp.
- Boissart, P., G. Guyot, and R. D. Jackson, 1990: Factors affecting the radiative temperature of vegetation canopy in applications of remote sensing in agriculture. *Applications of Remote Sensing in Agriculture*, M. D. Steven and J. A. Clark, Eds., Butterworth, 45–72.
- Brogniez, G., J. C. Buriez, V. Giraud, F. Parol, and C. Vanbauce, 1995: Determination of effective emittance and a radiatively equivalent microphysical model of cirrus from ground-based and satellite observations during the International Cirrus Experiment: The 18 October 1989 case study. *Mon. Wea. Rev.*, **123**, 1025–1036.
- Clough, S. A., F. X. Kneizys, and R. W. Davies, 1989: Line shape and the water vapor continuum. *Atmos. Res.*, **23**, 229–241.
- , M. J. Iacono, and J. L. Moncet, 1992: Line-by-line calculations of atmospheric fluxes and cooling rates: Application to water vapor. *J. Geophys. Res.*, **97**, 15 761–15 785.
- Dubuisson, P., J. C. Buriez, and Y. Fouquart, 1996: High spectral resolution solar radiative transfer in absorbing and scattering media: Application to the satellite simulation. *J. Quant. Spectros. Radiat. Transfer*, **55**, 103–126.
- Flamant, P. H., G. Brogniez, M. Desbois, Y. Fouquart, J. F. Flobert, J. C. Vanhouette, and U. N. Singh, 1989: High altitude cloud observations by ground-based lidar, infrared radiometer and Me-teosat measurements. *Ann. Geophys.*, **7**, 1–10.
- Fouquart, Y., B. Bonnel, G. Brogniez, J. C. Buriez, L. Smith, J. J. Morcrette, and A. Cerf, 1987: Observations of Saharian aerosols: Results of ECLATS field experiment. Part II: Broadband radiative characteristics of the aerosols and vertical radiative flux divergence. *J. Climate Appl. Meteor.*, **26**, 38–52.
- François, C., and C. Ottlé, 1994: Comparaison of different atmospheric correction algorithms with the ATSR/ERS-1 infrared radiometer. *Proc. 6th Int. Colloquium Physical Measurements and Signatures in Remote Sensing*, Val d'Isère, France, CNES/NASA, 57–64.
- Giver, L. P., C. Chackerian Jr., and P. Varanasi, 2000: Visible and near-infrared H<sub>2</sub>O line intensity corrections for Hitran-96. *J. Quant. Spectros. Radiat. Transfer*, **66**, 101–105.
- Han, Y., J. A. Shaw, H. Churnside, P. D. Brown, and S. A. Clough, 1997: Infrared spectral radiance measurements in the tropical Pacific atmosphere. *J. Geophys. Res.*, **102**, 4353–4356.
- Kneizys, F. X., E. P. Shettle, L. W. Abreu, J. H. Chetwynd, G. P. Anderson, W. O. Gallery, J. E. A. Selby, and S. A. Clough, 1988: Atmospheric transmittance/radiance: Computer code LOW-TRAN 7. Air Force Geophysics Laboratory Rep. AFGL-TR-88-0177, Environmental Research Paper, 1010, 137 pp.
- Legrand, M., C. Pietras, G. Brogniez, M. Haefelin, N. K. Abuhassan, and M. Sicard, 2000: A high-accuracy multiwavelength radiometer for in situ measurements in the thermal infrared. Part I: Characterization of the instrument. *J. Atmos. Oceanic Technol.*, **17**, 1203–1214.
- Lorenz, D., 1968: Temperature measurements of natural surfaces using infrared radiometers. *Appl. Opt.*, **7**, 1705–1710.
- Masuda, K., T. Takashima, and Y. Takayama, 1988: Emissivity of pure and sea waters for the model sea surface in the infrared window regions. *Remote Sens. Environ.*, **24**, 313–329.
- McClatchey, R. A., R. W. Fenn, J. E. A. Selby, F. E. Volz, and J. S. Garing, 1971: Optical properties of the atmosphere (revised). Air Force Cambridge Research Laboratory Rep. AFCRL-71-0279, Environmental Research Paper 354, 85 pp.
- Mutlow, C. T., A. M. Zavadsky, I. J. Barton, and D. T. Llewellyn-Jones, 1994: Sea surface temperature measurements by the along-track scanning radiometer on the ERS-1 satellite: Early results. *J. Geophys. Res.*, **99**, 22 575–22 588.
- Nerry, F., J. Labed, and M. P. Stoll, 1990: Spectral properties of land surfaces in the thermal infrared band. *J. Geophys. Res.*, **95**, 7027–7044.
- Platt, C. M. R., and A. C. Dilley, 1979: Remote sounding of high clouds: II. Emissivity of cirrostratus. *J. Appl. Meteor.*, **18**, 1144–1150.
- Rothman, L. S., and Coauthors, 1998: The HITRAN molecular spectroscopic database and HAWKS (HITRAN Atmospheric station). *J. Quant. Spectros. Radiat. Transfer*, **60**, 665–710.
- , K. Chance, J. Schroeder, and A. Goldman, 2001: New edition of HITRAN database. *Proc. 11th ARL Science Team Meeting*, Atlanta, Georgia, ARM, 1–7.
- Saunders, P. M., 1967: Aerial measurement of sea surface temperature in the infrared. *J. Geophys. Res.*, **72**, 4109–4117.
- Saunders, R. W., and P. J. Minnett, 1990: The measurement of sea surface temperature from C-130. Royal Aircraft Establishment at Farnborough, Meteorological Research Flight Internal Note 52, 12 pp.
- Schmugge, T. J., F. Becker, and L. Zhao-Liang, 1991: Spectral emissivity variations observed in airborne surface temperature measurements. *Remote Sens. Environ.*, **35**, 95–104.
- Seguin, B., J. P. Lagouarde, L. Savane, 1991: The assessment of regional crop water conditions for meteorological satellite thermal infrared data. *Remote Sens. Environ.*, **35**, 141–148.
- Tobin, D. C., and Coauthors, 1999: Downwelling spectral radiance observations at the SHEBA ice station: Water vapor continuum measurements from 17–26 micrometer. *J. Geophys. Res.*, **104**, 2081–2092.
- Vermeulen, A., 1996: Caractérisation des aérosols à partir de mesures optiques passives au sol: Apport des luminances totale et polarisée dans le plan principal. Ph.D. thesis no. 1171, Université des Sciences et Technologies de Lille, France, 195 pp.
- Weiss, M., 1971: Airborne measurements of Earth surface temperatures (Ocean and Land) in the 10–12  $\mu\text{m}$  and 8–14  $\mu\text{m}$  regions. *Appl. Opt.*, **10**, 1280–1287.